Case Studies in Thermal Engineering 67 (2025) 105808

Contents lists available at ScienceDirect

Case Studies in Thermal Engineering

journal homepage: www.elsevier.com/locate/csite

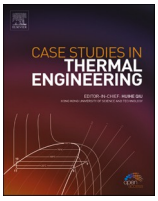

Enhancing solar thermoelectric generator performance using metal oxide layer absorbers under concentrated solar radiation

Abdelkader Rjafallah *, Daniel Tudor Cotfas, Petru Adrian Cotfas

Electrical Engineering and Computer Science Faculty, Transilvania University of Brasov, 500036, Brasov, Romania

ARTICLE INFO

Keywords:
Solar energy harvesting
Solar thermoelectric generators (STEGs)
Solar absorber (SA)
Metal oxides layer (MOL)
Graphite layer (GS)
Numerical 3D simulation
COMSOL Multiphysics

ABSTRACT

Solar Thermoelectric Generators (STEGs) hold promise for sustainable energy, with ongoing efforts to enhance efficiency through advanced thermal absorbers. This study evaluates the performance of STEGs using graphite sheet (GS) and metal oxides layer (MOL) absorbers under solar concentrations of 20, 40, 60, and 80 suns. Performance metrics, including short-circuit current (Isc), open-circuit voltage (Voc), maximum power output (Pmax), and efficiency (η), were measured experimentally using the KIRAN-42 solar simulator and compared with COMSOL Multiphysics simulations. The MOL-based STEG outperformed the GS-based counterpart, achieving Pmax (η) values of 0.559 W (1.75 %), 1.818 W (2.84 %), 3.071 W (3.2 %), and 3.762 W (2.94 %) at 20, 40, 60, and 80 suns, respectively, compared to 0.308 W (0.96 %), 1.120 W (1.75 %), 1.984 W (2.1 %), and 2.670 W (2.1 %) for the GS-based STEG. Experimental and simulation discrepancies were minimal at lower concentrations (1.9 % and 6.4 % at 20 suns) but increased at 80 suns (32.4 % and 41.7 %). Both approaches showed strong linear correlations between Pmax and solar concentration ($R^2 > 0.98$). Low RMSE values (0.45 for GS, 0.81 for MOL) further validated the models. This study underscores the superior performance of MOL absorbers and provides insights for optimizing STEG designs.

Nomenclature

Symbol	Definition	SI Unit
A	Cross-sectional area	m^2
C_p	Specific heat capacity	J/(kg • K)
$\vec{D}$	Electric displacement field	C/m^2
$\vec{E}$	Electric field intensity	V/m
ε	Dielectric permittivity	F/m
ε_r	Relative permittivity	–
h	Height	m
I	Electric current	A
$\vec{J}$	Current density	A/m^2
k, K	Thermal conductivity	W/(m • K)
L	Length	m
N	Number of p- and n-type leg pairs	–

(*continued on next page*)

* Corresponding author.
E-mail address: abdelkader.rjafallah@unitbv.ro (A. Rjafallah).

https://doi.org/10.1016/j.csite.2025.105808
Received 4 November 2024; Received in revised form 9 January 2025; Accepted 21 January 2025
Available online 29 January 2025

(*continued*)

Symbol	Definition	SI Unit
p	Peltier coefficient	V
P	Electrical power	W
$\vec{q}$	Heat flux	W/m^2
$\dot{q}$	Power density	W/m^3
Q	Heat	W
R	Electrical resistance	Ω
R^2	Coefficient of determination	–
r	Electrical resistivity	Ω • m
ρ	Density	kg/m^3
S	Seebeck coefficient	V/K
σ	Electrical conductivity	S/m
t	Time	s
T	Absolute temperature	K
ΔT	Temperature difference	K or °C
V	Electric potential	V
W	Width	m
α	Absorbance coefficient	–
η	Conversion efficiency	–
$\vec{\nabla}$	Nabla operator	–
Subscripts		
av	Average	
c	Cold side	
Cu	Copper	
GS	Graphite sheet	
h	Hot side	
in	Internal resistance	
max	maximum	
MOL	Metal oxides layer	
n	n-type leg	
oc	Open-circuit	
p	p-type leg	
Pitch	distance between p- and n-type legs	
QC	Quasi-crystal alloy	
s	Solar irradiance	
sc	Short-circuit	
Abbreviations		
3D	Three Dimensional	
BP	Black Paint absorbent layer	
CSP	Concentrated solar power	
PV	Photovoltaic	
PVT	Photovoltaic-thermal systems	
RMSE	Root mean square error	
SSA	Spectrally Selective Absorber	
STEG	Solar Thermoelectric Generator	
TEC	Thermoelectric Cooler	
TEG	Thermoelectric Generator	
Chemical formulas		
Bi_2Te_3	Bismuth Telluride	
$Ca_3Co_4O_3$	Calcium Cobalt Oxide	
$CaMnO_3$	Calcium Manganate	
CNT	Carbon Nanotube	
$CoSb_3$	Skutterudite	
Fe_2O_3	Iron(III) Oxide	
MnO_2	Manganese Dioxide	

1. Introduction

With the progressive exhaustion of fossil fuel reserves, sustainable and renewable energy sources are becoming increasingly important, prompting researchers to investigate novel and efficient energy harvesting technologies to expedite the energy transition [1–3]. Renewable energy sources are characterized by their inexhaustibility and environmental friendliness [4,5]. Among these, solar energy is considered a particularly important [6,7].

Various renewable energy technologies harness sunlight to generate electricity, thermal energy, or both. Photovoltaic (PV) systems, such as solar panels, which use the photovoltaic effect to directly convert sunlight into electricity [8,9]. Solar-thermal power systems, often called concentrated solar power (CSP) systems, first convert solar radiations into thermal energy, which is then used to generate

electricity [10–14]. Photovoltaic-thermal (PVT) systems are hybrid technologies that simultaneously produce both electricity and thermal energy [15]. Solar thermoelectric generators (STEGs) convert heat from sunlight directly into electricity [16].

STEGs are thermoelectric generators (TEGs) specifically designed to convert solar energy directly into electricity [17]. By using solar collectors, solar radiation is concentrated on the hot side of the TEGs, providing the solar thermal energy, which is then converted into electricity through the Seebeck effect [18,19]. "TEGs offer several advantages, including direct energy conversion, high reliability, silent operation, long lifespan, zero emissions, and the absence of moving parts" according to Refs. [20,21]. These attributes make TEGs ideal for applications such as waste heat recovery, remote low-power systems, space applications, and hybrid PV-TEG systems [22,23].

Enhancing STEG performance involves optimizing several parameters, including the thermal conductivity, absorptivity, and emissivity of the heat collector and the efficiency of the heat sink. Improving the heat collector's thermal conductivity and absorptivity while minimizing its emissivity increases input energy and overall efficiency [24]. Additionally, applying a high-quality thermal absorber to the hot side can further boost heat input, thereby enhancing energy conversion efficiency [25–27].

Mahmoudinezhad et al. [24] evaluated the performance of an oxide-based STEG with and without a graphite sheet (GS) affixed to the TEG's hot side under varying solar concentrations. They reported that the temperatures of the hot and cold sides of the TEG with the GS under 128 suns were nearly the same as those of the TEG without the GS under 292 suns. Additionally, the open-circuit voltage and short-circuit current of the TEG with the GS under 107 suns were 1.56 V and 1.21 A, respectively, compared to 1.5 V and 1.18 A for the TEG without the GS under 252 suns. Yadav et al. [28] conducted an experimental analysis of solar energy harvesting using a thermoelectric module (TEC 12706, 40 mm × 40 mm x 3.9 mm) coated with varying thicknesses (3, 3.5, 4.5, and 6 μm) of carbon soot obtained from direct exposure to a candle flame. The STEG with 6 μm thick carbon soot coating generated a short-circuit current of 14 mA, an open-circuit voltage of 1.5 V, and a maximum power output of 10.2 mW for a temperature difference of 39.9 °C, compared to 2.2 mA, 0.22 V, and 0.24 mW for the uncoated module at a temperature difference of 8.8 °C. This represented a sixfold increase in both open-circuit voltage and short-circuit current. Later, Mahmoudinezhad et al. [29] conducted numerical simulations using the finite volume method to analyze the dynamic response of a Bi_2Te_3-based STEG, with and without a GS, under varying solar radiation patterns. They reported that the maximum power generated by the STEG with the GS was nearly 2.5 times higher than that of the STEG without the GS, due to the greater amount of energy absorbed by the GS. Additionally, the efficiency of the STEG with the GS (3.3 %) was 2.53 times greater than that of the STEG module without the GS (1.3 %). Silva Oliveira et al. [30] conducted an experimental study to evaluate the performance of a STEG with a copper-based solar absorber coated with a quasicrystal (QC) alloy, comparing it to a STEG with a copper-based solar absorber coated with black paint (BP). The QC-based STEG produced an output voltage of 3 V and stored surplus energy (up to 1.38 J) in a 100-mF supercapacitor per day using a power management system. Additionally, the QC-based STEG generated 28.6 % more energy than the BP-based STEG and fully charged the supercapacitor around 2 h earlier. Sun et al. [31] conducted a pioneering study predicting the dynamic performance of a STEG under various solar concentration ratios throughout the entire day. The simulation spanned 660 min, and the study reported average daytime output power of 0.53 W, 2.01 W, 4.15 W, 6.70 W, 9.71 W, and 13.16 W at concentration levels of 25, 50, 75, 100, 125, and 150 suns, respectively. The corresponding mean daytime conversion efficiencies were 1.47 %, 2.80 %, 3.86 %, 4.69 %, 5.44 %, and 6.15 %. The maximum output power reached 17.70 W, with a peak conversion efficiency of 7.26 % at 238 min, under a concentration ratio of 150 suns, which correlates to a solar heat absorption of 208.48 W.

This paper focuses on simulating an entire STEG system with two different thermal absorbers: a commercial adhesive GS and a metal oxides layer (MOL), which was fabricated using a direct spray deposition technique on the hot side of the STEG at temperatures below 90 °C. Experiments and corresponding COMSOL simulations were conducted for STEGs with both absorbers under four levels of concentrated solar radiation (20, 40, 60, and 80 suns). The I-V and P-V curves of the STEGs were measured using the capacitor technique, and solar concentrations were achieved using the KIRAN-42 simulator. Key parameters, including I_{sc}, V_{oc}, and P_{max}, were used to compare experimental and simulated results.

The novelty and contributions of this paper are as follows.

- A comparative study of STEG performance incorporating both a GS and a MOL under varying concentrated illumination conditions, ranging from 20 to 80 suns.
- Simulation-based verification of the behavior of STEGs incorporating either a GS or a MOL under various light concentrations levels.

The remainder of the paper is organized as follows: Section 2 outlines the materials and methods used for simulating and experimenting with STEGs featuring GSs and MOLs on their hot sides under various concentrated solar radiations. In this regard, 3D models were constructed using COMSOL Multiphysics software, which relies on the finite element method, and simulated under different concentrated light conditions. This section also presents the assumptions and boundary conditions considered in this study, along with the equations governing the thermoelectric behavior of the STEGs. Furthermore, a grid-independent study was performed to investigate the effect of mesh size on model outputs. The experimental setup is also described. Section 3 outlines the results derived from the simulations and experiments, including analysis, discussion, and comparison of both sets of results. Section 4 outlines the conclusions derived from this study and provides insights for future research directions.

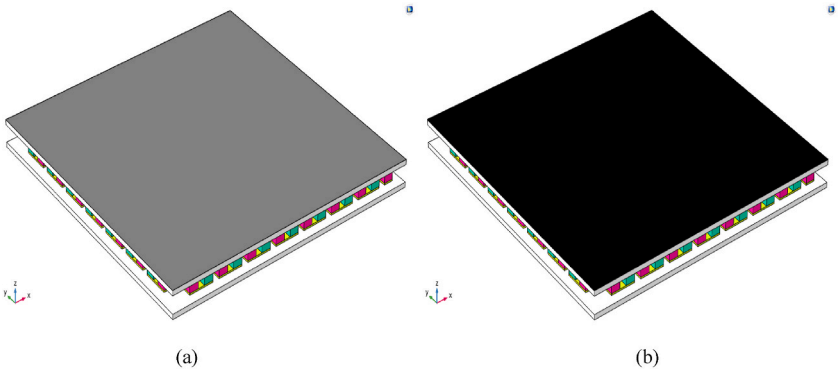

Fig. 1. Schematic of the solar thermoelectric generator (STEG) comprising two ceramic plates, 255 copper interconnectors, and 127 p- and n-type Bismuth Telluride leg pairs, featuring: (a) a 25 μm-thick graphite sheet (GS) absorber, and (b) an 87 μm-thick metal oxides layer (MOL) absorber.

Table 1
Geometric dimensions of the components in the simulated STEG model, including alumina ceramic plates, copper interconnectors, thermoelectric legs, graphite sheet (GS), and metal oxides layer (MOL).

Name	Value (mm)	Description
L_{TEG}	40	TEG module length
W_{TEG}	40	TEG module width
h_{TEG}	3.3	TEG module height
$L_{Alumina}$	40	Ceramic plates length
$W_{Alumina}$	40	Ceramic plates width
$h_{Alumina}$	0.6	Ceramic plates height
L_{Cu}	3.8	Copper interconnectors length
W_{Cu}	1.4	Copper interconnectors width
h_{Cu}	0.2	Copper interconnectors height
L_{Leg}	1.4	Legs length
W_{Leg}	1.4	Legs width
h_{Leg}	1.7	Legs height
d_{Pitch}	1	Distance between legs
L_{GS}	40	GS length
W_{GS}	40	GS width
h_{GS}	25×10^{-3}	GS height
L_{MOL}	40	MOL length
W_{MOL}	40	MOL width
h_{MOL}	87×10^{-3}	MOL height

2. Materials and methods

2.1. Solar thermoelectric generator (STEG)

This study investigates the performance of solar thermoelectric generators (STEGs) integrated with either a graphite sheet (GS) or a metal oxides layer (MOL) as solar absorbers, under varying levels of concentrated solar illumination ranging from 20 to 80 suns.

The STEG performance was simulated using COMSOL Multiphysics software under these illumination conditions. A three-dimensional model of a thermoelectric generator (TEG) module, adapted from prior research [16], was customized and slightly modified to align with the specific module used in this study. The TEG module, measuring 40 mm × 40 mm × 3.3 mm, consists of two ceramic plates, 255 copper interconnectors, 127 p- and n-type Bismuth Telluride leg pairs, and either a 25 μm-thick graphite sheet or an 87 μm-thick metal oxides layer integrated on its hot side (see Fig. 1).

Table 1 outlines the geometric dimensions of all components in the simulated STEG model, including the overall module dimensions, ceramic plates, copper interconnectors, graphite sheet, metal oxides layer, thermoelectric legs, the number of leg pairs, and the spacing between them.

Bismuth Telluride (Bi_2Te_3) was selected as the thermoelectric material for this study because its suitability for low-temperature applications, with a hot-side temperature not exceeding 250 °C. Bi_2Te_3 and its composites are widely recognized as optimal thermoelectric materials for temperatures below 250 °C, exhibiting a good figure of merit within this range. In addition, Bi_2Te_3 is extensively utilized in commercial TEG modules and remains a primary focus in academic research. These attributes made Bi_2Te_3-based TEG modules the ideal choice for this study.

The thermoelectric properties of Bi_2Te_3, including the Seebeck coefficient, electrical conductivity, and thermal conductivity, are highly temperature-dependent, as illustrated in Fig. 2. Unlike previous studies that treated these properties as constants regardless of

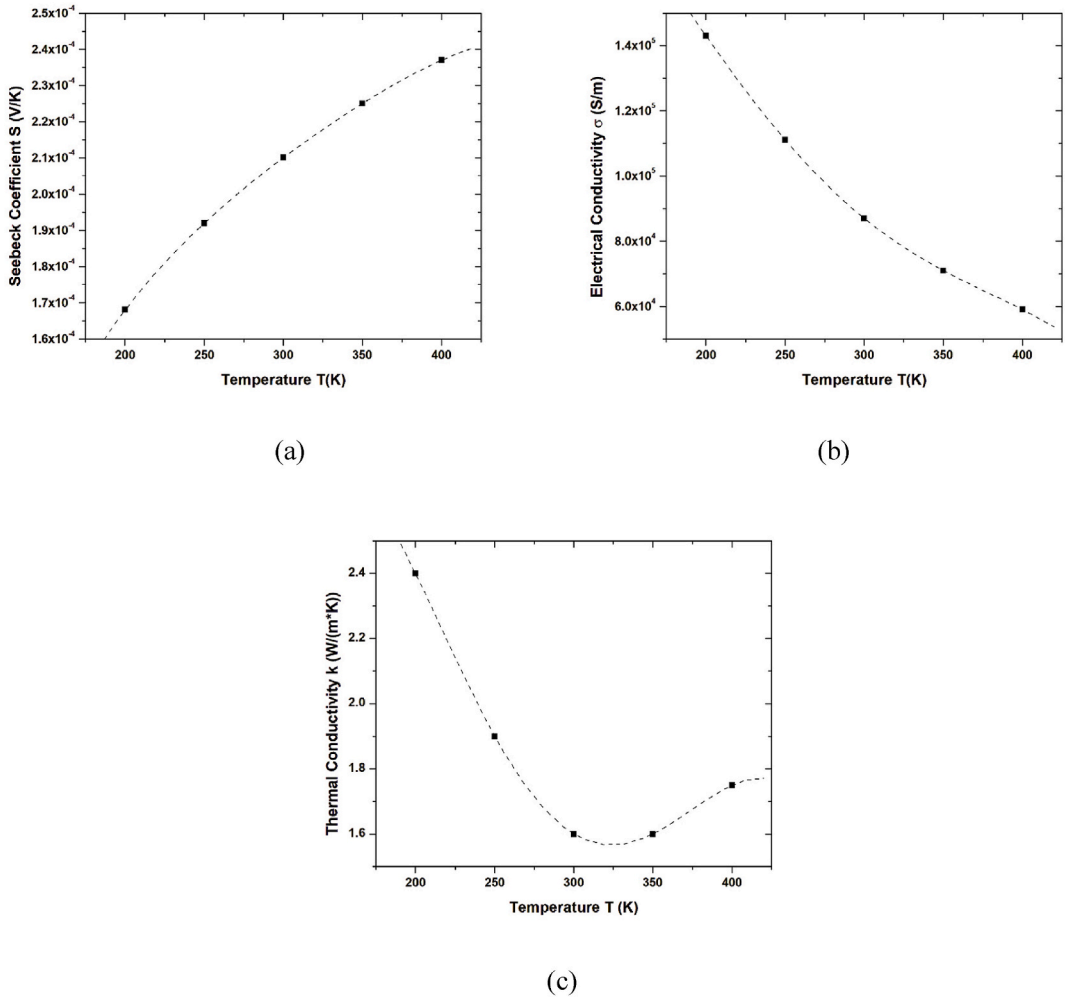

Fig. 2. Temperature-dependent profiles of (a) Seebeck coefficient, (b) electrical conductivity, and (c) thermal conductivity for Bismuth Telluride (Bi_2Te_3) thermoelectric materials [32].

Table 2
Material properties employed in the simulations [32,33].

Materials	Thermal Conductivity κ (W/(m • K))	Electrical conductivity σ (S/m)	Specific heat capacity C_p (J/(kg • K))	Density ρ (kg/m^3)	Relative permittivity ε_r	Seebeck Coefficient S (V/K)
MOL	9.9	–	640	5120	–	0
GS	1600	–	643	1900	–	0
Ceramic plates	27	–	900	3900	–	0
Copper conductors	400	5.998×10^7	385	8940	1	6.5×10^{-6}
Bi_2Te_3						
- p-type	κ(T) Fig. 2c	σ(T) Fig. 2b	154	7700	1	+S(T) Fig. 2a
- n-type						-S(T) Fig. 2a

temperature variations—often resulting in less accurate simulation outcomes—this study incorporates the temperature dependency of Bi_2Te_3's properties. This approach is essential for accurately simulating STEG performance under varying illumination levels, as the hot-side temperature changes with each level.

The temperature-dependent properties of Bi_2Te_3, sourced from Ref. [32], along with the material properties of the graphite sheet and metal oxides layer, were incorporated into the numerical model. Properties of additional components, such as ceramic plates and copper interconnectors, were already available in the COMSOL Multiphysics Materials Library [33]. Table 2 provides a detailed overview of the material properties used in the simulations.

2.2. Assumptions and boundary conditions

The simulations of the STEG with either a GS or a MOL under varying levels of solar concentration were conducted based on the following assumptions and boundary conditions.

- The simulations employed the following physics interfaces: Heat Transfer in Solids, Surface-to-Surface Radiation, Electric Currents, and Electrical Circuit.
- The analysis was performed under steady-state conditions.
- The STEGs were considered thermally isolated, with no heat exchange with the surroundings except for thermal dissipation from the upper surface of the TEG modules via radiation.
- Convective and radiative heat transfer between the p- and n-type legs was neglected.
- Thermal and electrical losses in the STEGs were assumed to be negligible.
- Electrical and thermal contact resistances were considered negligible, assuming perfect connections between all components of the TEG module.
- The GS, MOL, alumina ceramics, copper conductors, and p- and n-type legs were treated as distinct homogenous substances with associated isotropic and constant thermophysical properties.
- The p- and n-type legs were made of Bismuth Telluride (Bi_2Te_3).
- The Seebeck coefficient, thermal conductivity, and electrical conductivity of the p- and n-type legs, were assumed to vary with temperature within the considered range (see Fig. 2a–c).

2.3. Governing equations

The thermoelectric behavior of a TEG module is governed by the following two coupled equations [34].

1. Conservation of heat energy:

$$\rho C_p \frac{\partial T}{\partial t} + \vec{\nabla} \cdot \vec{q} = \dot{q} \tag{1}$$

where ρ is the density (kg/m^3), C_p is the specific heat capacity (J/(kg • K)), T is the temperature (K), $\vec{q}$ is the heat flux (W/m^2), and $\dot{q}$ represents the heat generation per unit volume (W/m^3).

2. Continuity of electric charge:

$$\vec{\nabla} \cdot \left(\vec{J} + \frac{\partial \vec{D}}{\partial t} \right) = 0 \tag{2}$$

where $\vec{J}$ is the current density (A/m^2) and $\vec{D}$ is the electric displacement field (C/m^2).

These equations are coupled by the following thermoelectric and dielectric constitutive equations [16].

- **Heat flux equation:**

$$\vec{q} = p\vec{J} - k\vec{\nabla}T \tag{3}$$

- **Current density equation:**

$$\vec{J} = \sigma\left(\vec{E} - S\vec{\nabla}T\right) \tag{4}$$

- **Electric displacement field equation:**

$$\vec{D} = \varepsilon\vec{E} \tag{5}$$

where.

- $p = ST$ (6) is the Peltier coefficient (V),
- S is the Seebeck coefficient (V/K),
- k is the thermal conductivity (W/(m • K)),
- σ is the electrical conductivity (S/m),

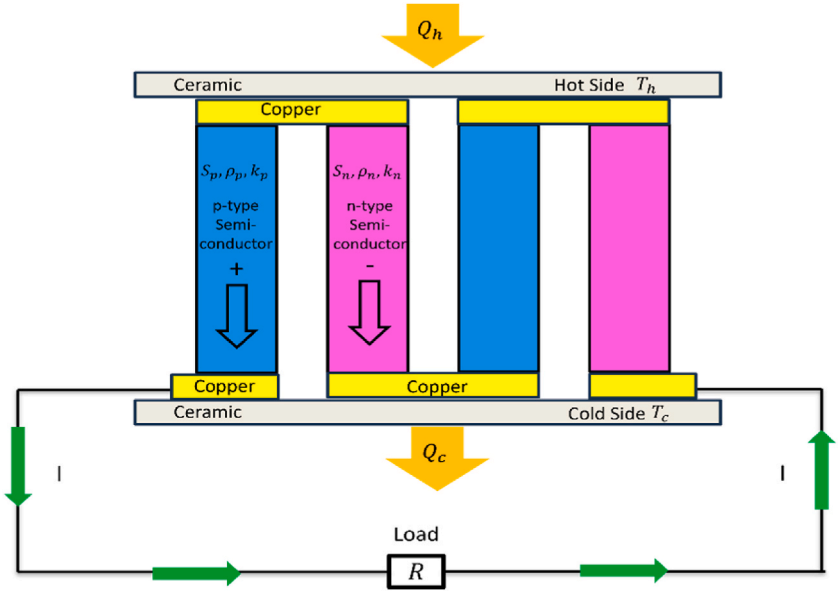

Fig. 3. Schematic diagram of a thermoelectric generator (TEG) module connected in series with an electrical load [22].

- $\vec{E} = -\vec{\nabla}V$ (7) is the electric field intensity (V/m),
- V is the electric scalar potential (V),
- ε is the dielectric permittivity (F/m).

Replacing Eqs. (3)–(7) in Eqs. (1) and (2) results in the following system of coupled thermoelectric equations [22]:

$$\rho C_p \frac{\partial T}{\partial t} - \vec{\nabla}\cdot(\sigma S T \vec{\nabla}V) - \vec{\nabla}\cdot\left(\sigma S^2 T \vec{\nabla}T\right) - \vec{\nabla}\cdot(k\vec{\nabla}T) - \sigma\vec{\nabla}V\cdot\vec{\nabla}V - \sigma S\vec{\nabla}T\cdot\vec{\nabla}V = 0 \tag{8}$$

$$\vec{\nabla}\cdot(\sigma\vec{\nabla}V) + \vec{\nabla}\cdot(\sigma S\vec{\nabla}T) + \vec{\nabla}\cdot\left(\varepsilon\vec{\nabla}\frac{\partial V}{\partial t}\right) = 0 \tag{9}$$

with the heat generation rate given by:

$$\dot{q} = \vec{J}\cdot\vec{E} = \sigma\vec{\nabla}V\cdot\vec{\nabla}V + \sigma S\vec{\nabla}T\cdot\vec{\nabla}V \tag{10}$$

Under steady-state conditions, the coupled thermoelectric equations simplify to Ref. [35]:

$$\vec{\nabla}\cdot(\sigma S T\vec{\nabla}V) + \vec{\nabla}\cdot\left(\sigma S^2 T\vec{\nabla}T\right) + \vec{\nabla}\cdot(k\vec{\nabla}T) + \sigma\vec{\nabla}V\cdot\vec{\nabla}V + \sigma S\vec{\nabla}T\cdot\vec{\nabla}V = 0 \tag{11}$$

$$\vec{\nabla}\cdot(\sigma\vec{\nabla}V) + \vec{\nabla}\cdot(\sigma S\vec{\nabla}T) = 0 \tag{12}$$

When a temperature difference ΔT is applied across the ends of a TEG module in open-circuit mode, the module generates an open-circuit voltage given by Ref. [36]:

$$V_{oc} = S\Delta T = S(T_h - T_c) \tag{13}$$

where T_h and T_c are the hot-side and cold-side temperatures, respectively.

When a TEG module is connected to an electrical load with resistance R (Fig. 3), the input heat at the hot side Q_h and the output heat at the cold side Q_c are given by Ref. [37]:

$$Q_h = ST_hI - \frac{1}{2}R_{in}I^2 + K\Delta T \tag{14}$$

$$Q_c = ST_cI + \frac{1}{2}R_{in}I^2 + K\Delta T \tag{15}$$

Where.

- S is the total Seebeck coefficient of all p- and n-type legs (defined in Eq. (16)),

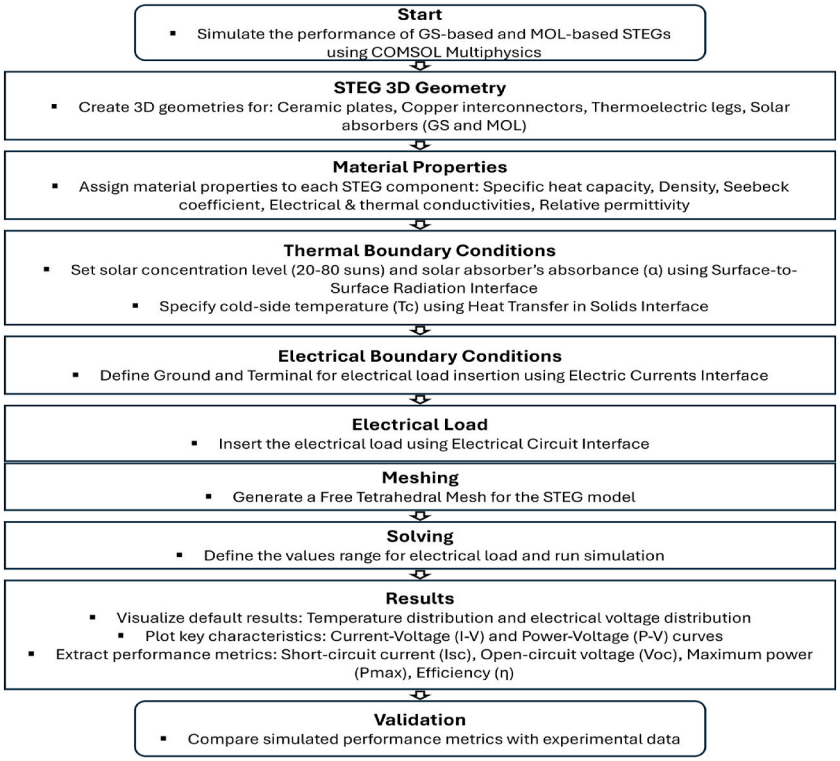

Fig. 4. Workflow of finite element method application in STEG simulation.

- R_{in} is the total internal resistance of all p- and n-type legs (defined in Eq. (17)),
- K is the total thermal conductance of all p- and n-type legs (defined in Eq. (18)),
- I is the electric current passing through the electrical load R (defined in Eq. (21)).

The expressions for S, R_{in}, and K are as follows:

$$S = N(S_p - S_n) \tag{16}$$

$$R_{in} = N\left[\frac{r_p L_p}{A_p} + \frac{r_n L_n}{A_n}\right] \tag{17}$$

$$K = N\left[\frac{k_p A_p}{L_p} + \frac{k_n A_n}{L_n}\right] \tag{18}$$

where.

- N is the number of p- and n-type leg pairs,
- S_p and S_n are the Seebeck coefficients of the p- and n-type legs, respectively,
- r_p and r_n are the electrical resistivities of the p- and n-type legs, respectively,
- k_p and k_n are the thermal conductivities of the p- and n-type legs, respectively,
- A_p and A_n are the cross-sectional areas of the p- and n-type legs, respectively,
- L_p and L_n are the lengths of the p- and n-type legs, respectively.

According to the first law of thermodynamics, the electric power P produced by the TEG module across the electrical load R is expressed as follows [38]:

$$P = Q_h - Q_c = S\Delta TI - R_{in}I^2 \tag{19}$$

Using Kirchhoff's voltage law, the electrical voltage V across the load R can be expressed as:

$$V = V_{oc} - R_{in}I = S\Delta T - R_{in}I \tag{20}$$

The electric current I passing through the load R can be written as:

Table 3
Grid-independence analysis for the graphite sheet (GS)-based and metal oxides layer (MOL)-based STEGs.

Element Size	Element Number	I_{sc} (A)	V_{oc} (V)	P_{max} (W)
GS-based STEG				
Coarse	96,085	0.52048	1.9670	0.31397
Normal	171,689	0.52047	1.9670	0.31397
Fine	489,230	0.52044	1.9670	0.31393
MOL-based STEG				
Coarse	95,941	0.66879	2.5565	0.52311
Normal	171,828	0.66877	2.5565	0.52310
Fine	488,807	0.66873	2.5565	0.52307

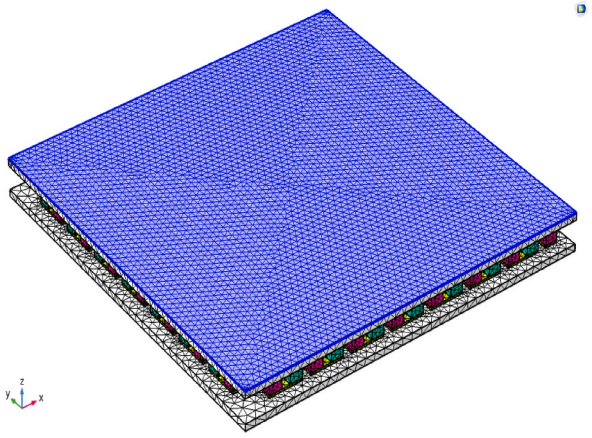

Fig. 5. Mesh generated using the free tetrahedral meshing technique for the graphite sheet (GS)-based solar thermoelectric generator (STEG).

$$I = \frac{V_{oc}}{R_{in} + R} = \frac{S\Delta T}{R_{in} + R} \tag{21}$$

Consequently, the electric power P delivered to the load R can be reformulated as follows:

$$P = RI^2 = R\left(\frac{S\Delta T}{R_{in} + R}\right)^2 \tag{22}$$

The maximum power P_{max} produced by the TEG module is achieved when the load resistance R matches the internal resistance of the TEG module ($R = R_{in}$). Under this condition, the maximum power is expressed as:

$$P_{max} = \frac{1}{4}\frac{(S\Delta T)^2}{R} \tag{23}$$

The efficiency η of the TEG module is defined as the ratio of the power output to the heat input, and is expressed as:

$$\eta = \frac{P_{out}}{Q_h} = \frac{RI^2}{ST_hI - \frac{1}{2}R_{in}I^2 + K\Delta T} \tag{24}$$

2.4. Workflow of finite element method application in STEG simulation

The workflow for simulating the performance of GS-based and MOL-based STEGs using COMSOL Multiphysics software is illustrated in Fig. 4. The process begins with creating a 3D geometry of the STEG using the drawing tools integrated into COMSOL. The model includes individual components such as two blocks for ceramic plates, 255 blocks for copper interconnectors, 254 blocks for thermoelectric legs, and a single block for the solar absorber (either GS or MOL).

Next, material properties for each STEG component are assigned, including specific heat capacity, density, Seebeck coefficient, electrical and thermal conductivities, and relative permittivity. Following this, thermal boundary conditions are specified: the solar concentration level (20–80 suns) and the absorber's absorbance coefficient (α) are defined using the Surface-to-Surface Radiation Interface, while the cold-side temperature is set using the Heat Transfer in Solids Interface.

Electrical boundary conditions are established by defining the Ground and Terminal for electrical load insertion using the Electric Currents Interface. The electrical load is then inserted into the model via the Electrical Circuit Interface.

The STEG model is discretized into finite elements using the Free Tetrahedral Mesh technique. A range of electrical load values is

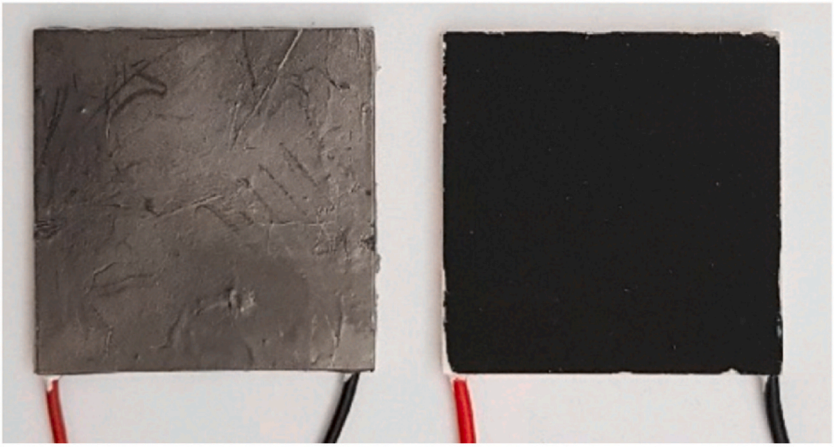

Fig. 6. (a) Solar thermoelectric generator (STEG) with a graphite sheet (GS) absorber; (b) STEG with a metal oxides layer (MOL) absorber [40].

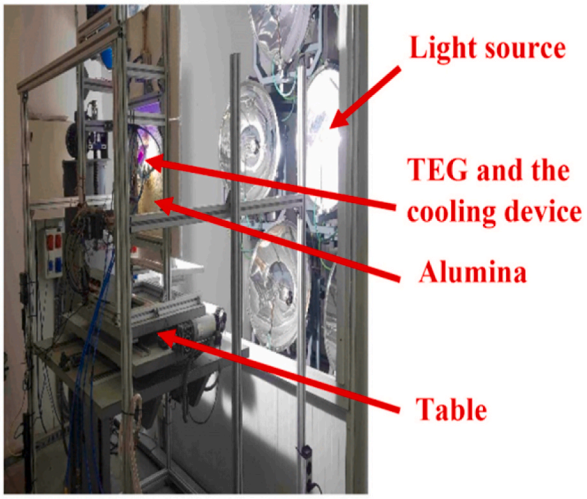

Fig. 7. Experimental setup for testing solar thermoelectric generators (STEGs) with a graphite sheet (GS) absorber or metal oxides layer (MOL) absorber under varying levels of concentrated solar irradiance [40].

specified, and the simulation is executed. Upon completion, default results such as temperature distribution and electrical potential distribution are visualized. Key performance characteristics, including Current-Voltage (I-V) and Power-Voltage (P-V) curves, are plotted.

Finally, critical performance metrics—such as short-circuit current (I_{sc}), open-circuit voltage (V_{oc}), maximum power (P_{max}), and efficiency (η)—are extracted from the I-V and P-V curves and compared to experimental data to validate the simulation results.

2.5. Grid-independence analysis

The analysis of mesh independence was conducted to determine the effect of mesh size on model outputs. Simulations of the STEGs were performed under the same concentrated light level (20 suns), with the cold side uniformly set to a temperature of 20 °C, using three different mesh sizes for each absorbent layer. Free tetrahedral element-based meshing was chosen as it is well-suited for complex and irregular geometries.

Table 3 presents the I_{sc}, V_{oc}, and P_{max} values obtained from simulations of the STEGs under the specified boundary conditions for three different mesh sizes for each absorbent layer (GS and MOL). The study revealed no significant changes in the model outputs, confirming grid independence. Based on the balance between computation time and resource compatibility, the element size "Normal" was chosen for subsequent simulations in this study. Fig. 5 illustrates the free tetrahedral mesh generated for the "Normal" element size.

Table 4
Experimental performance results for the graphite sheet (GS)-based and metal oxides layer (MOL)-based STEGs under four levels of concentrated solar irradiance: 20 suns (T_c = 20 °C), 40 suns (T_c = 30 °C), 60 suns (T_c = 41 °C), and 80 suns (T_c = 49 °C).

	I_s (W/m^2)	P_{in} (W)	T_h (°C)	T_c (°C)	I_{sc} (A)	V_{oc} (V)	P_{max} (W)	η (%)	Gain (%)
GS-based STEG	20,000	32	52	20	0.710	1.831	0.308	0.96	–
	40,000	64	82	30	1.267	3.482	1.120	1.75	–
	60,000	96	113	41	1.602	4.854	1.984	2.1	–
	80,000	128	152	49	1.786	5.555	2.670	2.1	–
MOL-based STEG	20,000	32	62	20	0.938	2.496	0.559	1.75	82
	40,000	64	110	30	1.557	4.655	1.818	2.84	62
	60,000	96	151	41	1.896	6.430	3.071	3.2	52
	80,000	128	178	49	2.058	7.316	3.762	2.94	40

2.6. Spectrally selective absorbers (SSAs)

The performance of the STEG can be enhanced by depositing a spectrally selective absorber (SSA) coating on its hot side to increase irradiance absorption. A SSA coating is a material deposited on surfaces, typically in solar energy applications, designed to absorb sunlight efficiently while minimizing heat loss through radiation. These coatings are engineered to have high absorption of solar radiation (which is primarily in the visible and near-infrared spectrum) and low emissivity in the infrared range, which reduces thermal radiation losses. This selective behavior enhances the efficiency of STEGs by maximizing the amount of solar energy converted into useable electricity while minimizing the energy lost as infrared radiation. In this study, two different SSAs were used: a 25 μm thick adhesive GS supplied by Panasonic was deposited on the hot side of one TEG module (Fig. 6a), while an 87 μm thick MOL, prepared in the Electronics and Computers Department at Transilvania University of Brasov, was deposited on the hot side of the other TEG module (Fig. 6b).

The MOL is developed through a two-step process: first, metal oxides (Iron(III) Oxide (Fe_2O_3), Manganese Dioxide (MnO_2), and additives) are synthesized using the sol-gel method with the incorporation of carbon nanotubes (CNTs). In the second step, the layer is deposited via a spray technique [39]. The detailed manufacturing process of the MOL is described in Refs. [40,41].

2.7. Experimental setup

The experiments were conducted at the IMDEA Energy Institute, Mostoles-Madrid, Spain. The experimental setup includes a Xenon lamp, STEGs with either a GS or a MOL, a water-cooled heat sink and a chiller, a Gardon sensor, an alumina shield, an electronic characterization system, and a three-direction movable table. The movable table allows precise positioning of the target (either the STEG or the Gardon sensor) relative to the lamp's focus (see Fig. 7).

The TEGs used are commercial TEC1-12710 modules supplied by STONECOLD. Each TEG module measures 40 mm × 40 mm × 3.3 mm and comprises two alumina ceramic plates, 255 copper interconnectors, and 127 pairs of p-type and n-type legs made of Bismuth Telluride (Bi_2Te_3) semiconductor material. The legs are rectangular in shape. Before being converted into STEGs, the TEG modules were tested to identify two units with equal internal resistance and nearly identical power output under the same conditions. A 25 μm thick adhesive GS (supplied by Panasonic) was deposited on the hot side of one TEG module, while an 87 μm thick MOL (prepared in the laboratory) was deposited on the hot side of the other TEG module.

A single Xenon lamp from the KIRAN-42 IMDEA High-Flux Solar Simulator was used to provide four levels of concentrated solar irradiance (20, 40, 60, and 80 suns), measured by a Gardon sensor. The irradiance intensity was varied by adjusting the distance between the Xenon lamp and the STEGs using a three-direction movable table, ensuring that the spectral distribution remained unchanged. The positions of the table were determined for each irradiance level using a Gardon sensor. An alumina sheet was used as a protective support, featuring a hole that allowed illumination of the hot side of the STEGs.

A water-cooled heat sink, made from copper with milled channels and measuring 80 mm × 90 mm × 10 mm, was used to cool the cold side of the STEGs. The water flow and temperature were kept quasi-constant throughout the experiments using a water chiller. Thermal grease and a tightening system with screws were employed to ensure optimal thermal contact between the STEG and the heat sink.

The temperature of the cold side of the STEGs was measured using three K-type thermocouples: one placed at the center and two positioned symmetrically, 1 cm away from the center. For the hot side, two K-type thermocouples were used, positioned 5 mm from the edges.

The electronic characterization system, utilizing the capacitor technique [5] and the NI cRIO 9074 platform [42] with appropriate Input/Output modules and a custom-designed electronic load, features four independent channels for measuring the current-voltage characteristics of the STEGs. This system captures I-V characteristics, temperatures, and provides real-time data on I_{sc}, V_{oc}, and P_{max}. The I-V characteristics, temperature measurements, and irradiance levels were monitored through software applications developed using NI LabVIEW.

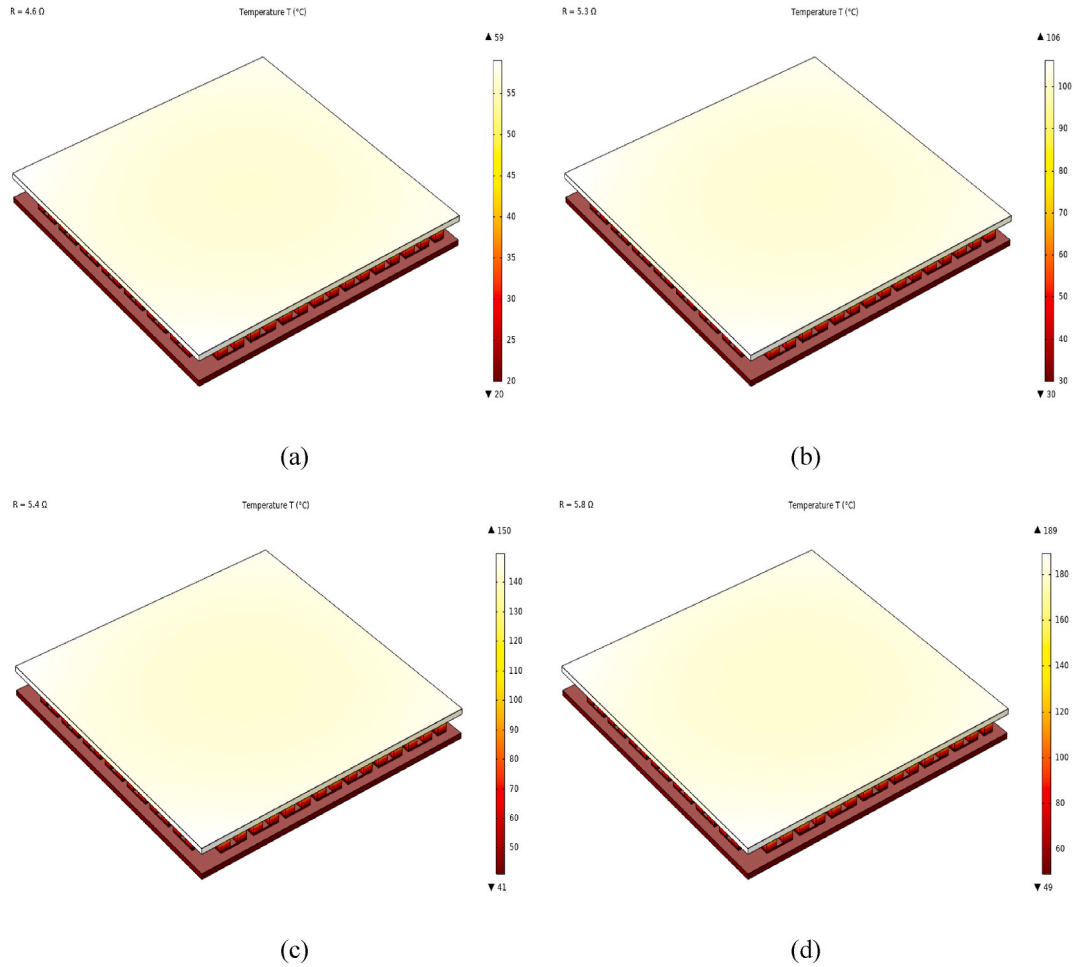

Fig. 8. Temperature distribution in the graphite sheet (GS)-based solar thermoelectric generator (STEG) under four levels of concentrated solar irradiance: (a) 20 suns with a cold-side temperature (T_c) of 20 °C, (b) 40 suns with T_c = 30 °C, (c) 60 suns with T_c = 41 °C, and (d) 80 suns with T_c = 49 °C.

3. Results and discussion

3.1. Experimental results

The I-V curves were measured for the GS-based STEG and the MOL-based STEG under four boundary conditions: 20 suns with T_c = 20 °C, 40 suns with T_c = 30 °C, 60 suns with T_c = 41 °C, and 80 suns with T_c = 49 °C. Measurements were taken at 20-s intervals, with the I_{sc} and V_{oc} results extracted from the I-V curves, and the corresponding P_{max} values were calculated. The final I-V characteristic recorded for each boundary condition was used as the representative I-V characteristic for both the GS-based STEG and the MOL-based STEG.

Table 4 presents the experimental I_{sc}, V_{oc}, and P_{max} results for the GS-based STEG and the MOL-based STEG under four boundary conditions: 20 suns with T_c = 20 °C, 40 suns with T_c = 30 °C, 60 suns with T_c = 41 °C, and 80 suns with T_c = 49 °C.

The experimental data revealed notable local similarities between the GS-based and MOL-based STEGs under varying solar concentrations. Despite the differences in solar absorbers, both configurations exhibited relatively close cold-side temperatures (T_c) at the same solar concentration levels. Furthermore, at higher solar concentrations (80 suns), their efficiencies converged toward similar values: 2.1 % for the GS-based STEG and 2.94 % for the MOL-based STEG [43]. Additionally, both STEGs demonstrated a linear relationship between solar concentration and key performance metrics, such as open-circuit voltage (V_{oc}) and maximum power output (P_{max}), with this linear trend remaining consistent across all irradiance levels [24].

The close cold-side temperatures, the narrowing efficiency gap at high irradiance levels, and the consistent linear trends suggest local similarities in performance. This indicates that as solar concentration increases, the absorber's material properties play a reduced role compared to the heat sink's capacity to dissipate excess heat. Moreover, the observed linear dependence of electrical behavior on solar concentration for both configurations implies that similar underlying physical principles govern their performance.

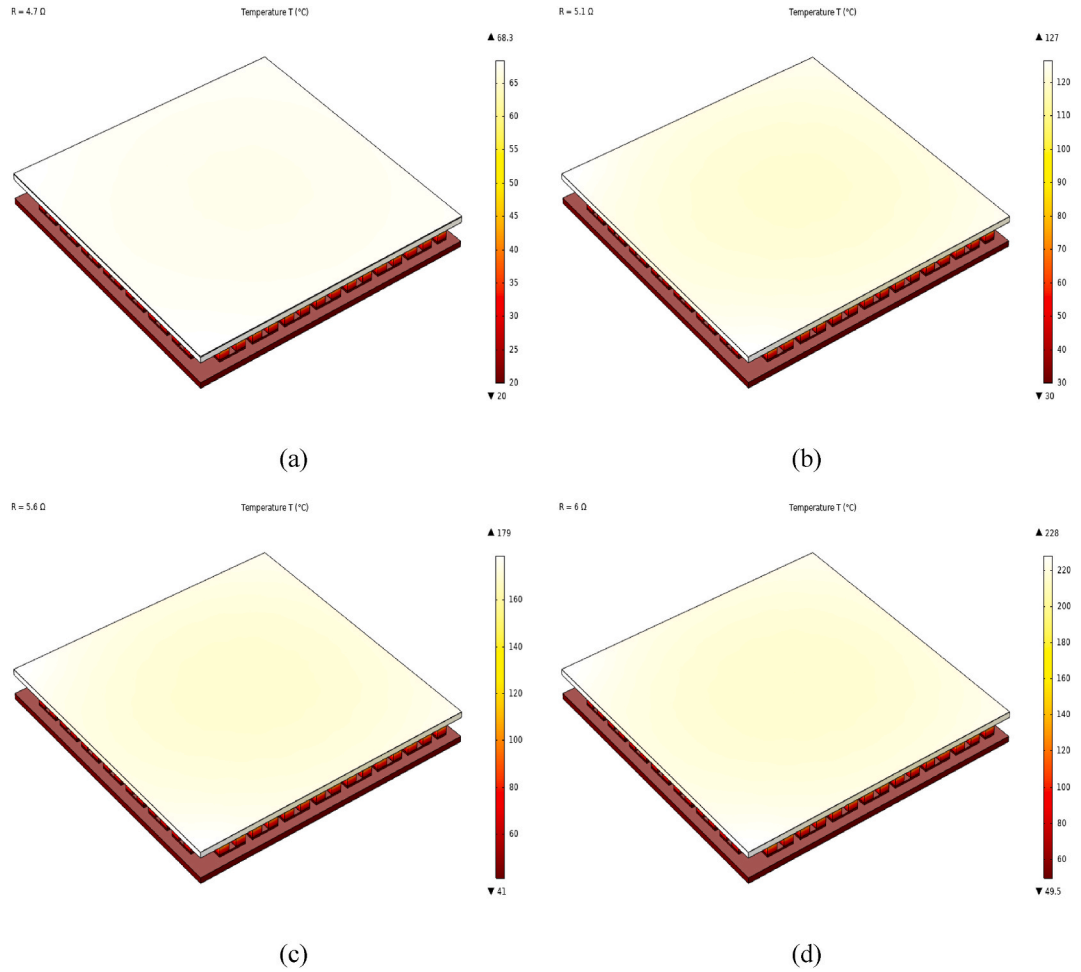

Fig. 9. Temperature distribution in the metal oxides layer (MOL)-based solar thermoelectric generator (STEG) under four levels of concentrated solar irradiance: (a) 20 suns with a cold-side temperature (T_c) of 20 °C, (b) 40 suns with $T_c = 30$ °C, (c) 60 suns with $T_c = 41$ °C, and (d) 80 suns with $T_c = 49$ °C.

Overall, the MOL-based STEG demonstrated superior performance in I_{sc}, V_{oc}, and P_{max} compared to the GS-based STEG. Specifically, for P_{max} (efficiency η), the GS-based STEG generated 0.308 W (0.96 %), 1.120 W (1.75 %), 1.984 W (2.1 %), and 2.670 W (2.1 %) under the respective conditions. In contrast, the MOL-based STEG generated 0.559 W (1.75 %), 1.818 W (2.84 %), 3.071 W (3.2 %), and 3.762 W (2.94 %) under the same conditions. These results show improvements in η of approximately 82 %, 62 %, 52 %, and 40 % for the MOL-based STEG compared to the GS-based STEG. Additionally, the P_{max} generated by the MOL-based STEG under 60 suns with $T_c = 41$ °C was higher than that generated by the GS-based STEG under 80 suns with $T_c = 49$ °C. This suggests that the MOL-based STEG under 60 suns can achieve a higher power output than the GS-based STEG under 80 suns, potentially allowing for a reduction in the size of the Fresnel lens and, consequently, the overall STEG system.

3.2. Simulation results

The objective of this paper is to simulate STEGs under four levels of concentrated solar irradiance (20, 40, 60, and 80 suns) and compare the simulation results with experimental data. The complete STEG system includes concentrated solar irradiation, a TEG module, and either a GS or a MOL. The measured solar irradiances applied to the hot sides of the STEGs, along with the corresponding temperatures on the cold side (as presented in Table 4), were used as inputs for the numerical models. The comparison between the simulated and experimental results focuses particularly on the I_{sc}, V_{oc}, and P_{max} outcomes.

Figs. 8 and 9 illustrate the temperature distributions across the STEGs with a GS and a MOL, respectively, under four levels of concentrated solar irradiance: 20 suns with $T_c = 20$ °C, 40 suns with $T_c = 30$ °C, 60 suns with $T_c = 41$ °C, and 80 suns with $T_c = 49$ °C.

A temperature difference of 48 °C was observed across the MOL-based STEG, while a temperature difference of 39 °C was observed across the GS-based STEG. This is due to the good absorbance of the MOL compared to that of the GS.

The I-V and P-V curves of the GS-based STEG and the MOL-based STEG, under four levels of concentrated solar irradiance: 20 suns

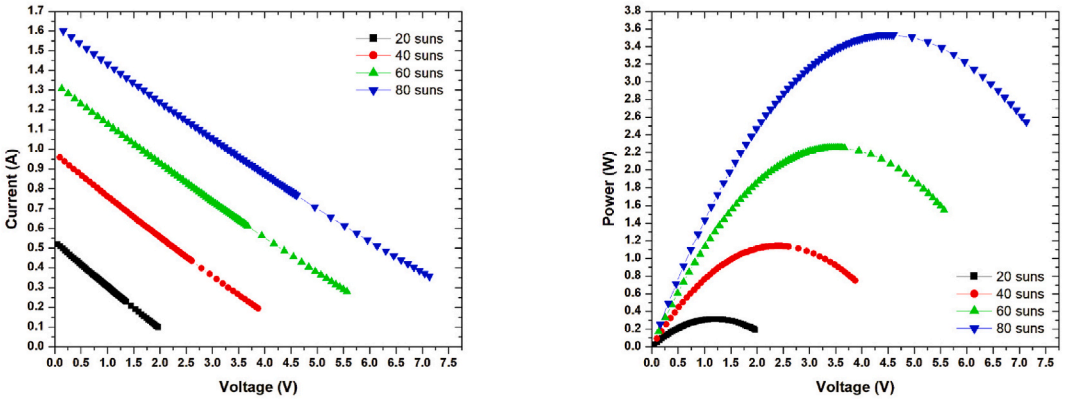

Fig. 10. Current-voltage (I–V) and power-voltage (P–V) characteristics of the graphite sheet (GS)-based solar thermoelectric generator (STEG) under four levels of concentrated solar irradiance: 20 suns with a cold-side temperature (T_c) of 20 °C, 40 suns with T_c = 30 °C, 60 suns with T_c = 41 °C, and 80 suns with T_c = 49 °C.

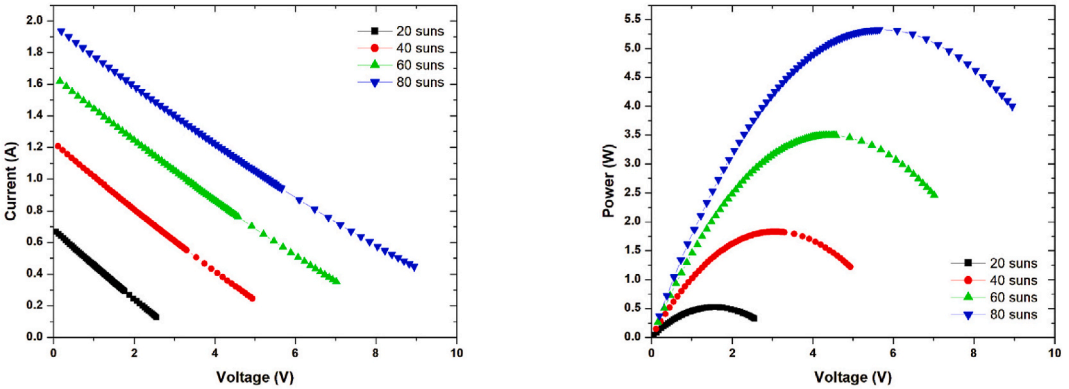

Fig. 11. Current-voltage (I–V) and power-voltage (P–V) characteristics of the metal oxides layer (MOL)-based solar thermoelectric generator (STEG) under four levels of concentrated solar irradiance: 20 suns with a cold-side temperature (T_c) of 20 °C, 40 suns with T_c = 30 °C, 60 suns with T_c = 41 °C, and 80 suns with T_c = 49 °C.

Table 5
Simulation results for the graphite sheet (GS)-based STEG under four levels of concentrated solar irradiance: 20 suns (T_c = 20 °C), 40 suns (T_c = 30 °C), 60 suns (T_c = 41 °C), and 80 suns (T_c = 49 °C).

	I_s (W/m^2)	P_{in} (W)	α	T_{max} (°C)	$T_{h,av}$ (°C)	T_c (°C)	I_{sc} (A)	V_{oc} (V)	P_{max} (W)	η
Exp.	20,000	32	–	–	52	20	0.710	1.831	0.308	0.96
Sim.			0.75	59	56.1	20	0.520 (−26.7 %)	1.967 (+7.4 %)	0.314 (+1.9 %)	0.98 (+2.1 %)
Exp.	40,000	64	–	–	82.5	30.5	1.267	3.482	1.120	1.75
Sim.			0.75	106	100.5	30	0.958 (−24.4 %)	3.872 (+11.2 %)	1.142 (+1.9 %)	1.78 (+1.7 %)
Exp.	60,000	96	–	–	113	41	1.602	4.854	1.984	2.1
Sim.			0.75	150	141.3	41	1.307 (−18.4 %)	5.568 (+14.7 %)	2.251 (+13.4 %)	2.3 (+9.5 %)
Exp.	80,000	128	–	–	152.5	49.5	1.786	5.555	2.670	2.1
Sim.			0.75	189	178.0	49	1.600 (−10.4 %)	7.131 (+28.4 %)	3.535 (+32.4 %)	2.7 (+28.5 %)

with T_c = 20 °C, 40 suns with T_c = 30 °C, 60 suns with T_c = 41 °C, and 80 suns with T_c = 49 °C, are depicted in Figs. 10 and 11, respectively.

Table 5 presents the simulation results for the GS-based STEG under four levels of concentrated solar irradiance, detailing the I_{sc}, V_{oc}, P_{max}, and η. Additionally, the table provides the maximum temperature (T_{max}) on the top surface of the GS and the average temperature ($T_{h,av}$) on the hot side of the STEG. The solar absorbance (α) of the GS, as defined in the numerical model, is also included.

A comparison of the simulated and experimental results for I_{sc}, V_{oc}, P_{max}, and η was performed. Under 20 suns with T_c = 20 °C, the simulated I_{sc} was 26.7 % lower, while the simulated V_{oc} and P_{max} were 7.4 % and 1.9 % higher, respectively. Under 40 suns with T_c = 30 °C, the simulated I_{sc} was 24.4 % lower, while the simulated V_{oc} and P_{max} were 11.2 % and 1.9 % higher, respectively. At 60 suns with T_c = 41 °C, the simulated I_{sc} was 18.4 % lower, while V_{oc} and P_{max} were 14.7 % and 13.4 % higher, respectively. Finally, under 80

Table 6
Simulation results for the metal oxides layer (MOL)-based STEG under four levels of concentrated solar irradiance: 20 suns ($T_c = 20$ °C), 40 suns ($T_c = 30$ °C), 60 suns ($T_c = 41$ °C), and 80 suns ($T_c = 49$ °C).

	I_s (W/m^2)	P_{in} (W)	α	T_{max} (°C)	$T_{h,av}$ (°C)	T_c (°C)	I_{sc} (A)	V_{oc} (V)	P_{max} (W)	η
Exp.	20,000	32	–		62.5	20	0.938	2.496	0.559	1.75
Sim.			0.98	68.3	66.7	20	0.669 (−28.7 %)	2.556 (+2.4 %)	0.523 (−6.4 %)	1.63 (−6.8 %)
Exp.	40,000	64	–		110	30.5	1.557	4.655	1.818	2.84
Sim.			0.98	127	119.2	30	1.207 (−22.5 %)	4.937 (+6.0 %)	1.829 (+0.6 %)	2.86 (+0.7 %)
Exp.	60,000	96	–		151.5	41	1.896	6.430	3.071	3.2
Sim.			0.98	179	167.9	41	1.617 (−14.7 %)	7.016 (+9.1 %)	3.495 (+13.8 %)	3.6 (+12.5 %)
Exp.	80,000	128	–		178.5	49.5	2.058	7.316	3.762	2.94
Sim.			0.98	228	213.5	49.5	1.936 (−5.9 %)	8.944 (+22.2 %)	5.330 (+41.7 %)	4.16 (+41.5 %)

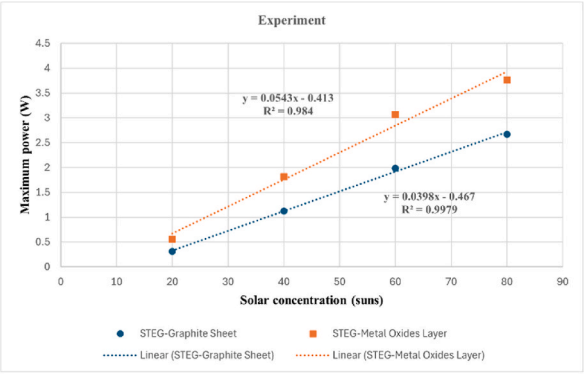

Fig. 12. Correlation between experimental maximum power output (P_{max}) and solar concentration for the graphite sheet (GS)-based and metal oxides layer (MOL)-based solar thermoelectric generators (STEGs).

suns with $T_c = 49$ °C, the simulated I_{sc} was 10.4 % lower, while V_{oc} and P_{max} were 28.4 % and 32.4 % higher, respectively.

The I_{sc} results showed that the discrepancy between simulated and experimental values decreased as irradiation increased, with the maximum difference being 26.7 % at 20 suns. In contrast, the difference for V_{oc} increased, with the largest deviation of 28.4 % occurring at 80 suns.

Regarding P_{max}, there was a minimal difference of 1.9 % between simulated and experimental values at lower irradiation levels (20 and 40 suns). However, at higher levels (60 and 80 suns), the differences increased to 13.4 % and 32.4 %, respectively.

As for η, the differences between simulated and experimental values were relatively small at lower irradiance levels (2.1 % at 20 suns and 1.7 % at 40 suns). However, at higher irradiance (60 and 80 suns), the discrepancies increased to 9.5 % and 28.5 %, respectively.

At each irradiation level, the discrepancy between the simulated and experimental I_{sc} and V_{oc} values could be attributed to differences in the measurement and simulation points. Specifically, the simulated I_{sc} values were not obtained at $V_{oc} = 0$ V because $R = 0$ is undefined for the electrical load in the numerical model. Instead, a non-zero resistance ($R \neq 0$) was defined, leading to consistently lower simulated I_{sc} values compared to the experimental ones. In contrast, the simulated V_{oc} values were taken at points higher than the experimental V_{oc} values, causing the simulated V_{oc} to consistently exceed the experimental values.

The variations in the differences between simulated and experimental P_{max} and η values with respect to irradiation levels could be attributed to temperature nonuniformities, which increase as the irradiation level rises. In real-world conditions, these nonuniformities are caused by irradiance fluctuations, whereas in the simulations, they were not taken into account. Overall, the simulations show good agreement with the experimental data.

Table 6 presents the simulation results for the MOL-based STEG under four levels of concentrated solar irradiance, detailing the I_{sc}, V_{oc}, P_{max}, and η. Additionally, the table includes the T_{max} on the top surface of the MOL and the $T_{h,av}$ on the hot side of the STEG. The α of the MOL, as defined in the numerical model, is also included.

A comparison of the simulated and experimental results for I_{sc}, V_{oc}, P_{max}, and η was performed. Under 20 suns with $T_c = 20$ °C, the simulated V_{oc} was 2.4 % higher, while the simulated I_{sc} and P_{max} were 28.7 % and 6.4 % lower, respectively. At 40 suns with $T_c = 30$ °C, the simulated I_{sc} was 22.5 % lower, while the simulated V_{oc} and P_{max} were 6.0 % and 0.6 % higher, respectively. At 60 suns with $T_c = 41$ °C, the simulated I_{sc} was 14.7 % lower, and the simulated V_{oc} and P_{max} were 9.1 % and 13.8 % higher, respectively. At 80 suns with $T_c = 49$ °C, the simulated I_{sc} was 5.9 % lower, while the simulated V_{oc} and P_{max} were 22.2 % and 41.7 % higher, respectively.

The I_{sc} results showed that the discrepancy between simulated and experimental values decreased as irradiation increased, with the largest difference of 28.7 % at 20 suns. Conversely, the difference in V_{oc} increased with irradiance, reaching a maximum deviation of 22.2 % at 80 suns.

Regarding P_{max}, the differences between simulated and experimental values were relatively small at lower irradiation levels (6.4 %

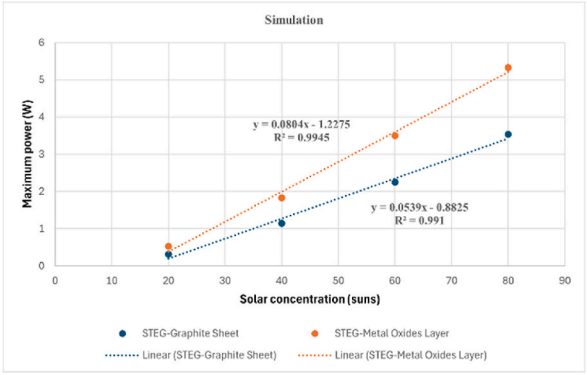

Fig. 13. Correlation between simulated maximum power output (P_{max}) and solar concentration for the graphite sheet (GS)-based and metal oxides layer (MOL)-based solar thermoelectric generators (STEGs).

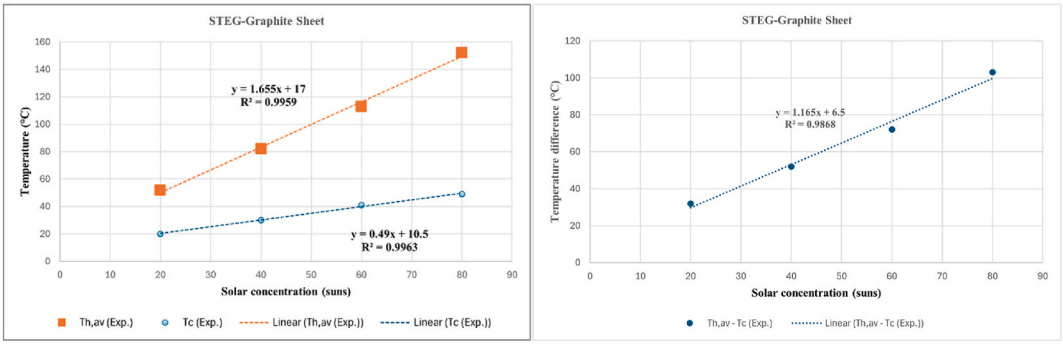

(a) (b)

Fig. 14. Variation of (a) hot-side and cold-side temperatures and (b) temperature difference as a function of solar concentration for the graphite sheet (GS)-based solar thermoelectric generator (STEG).

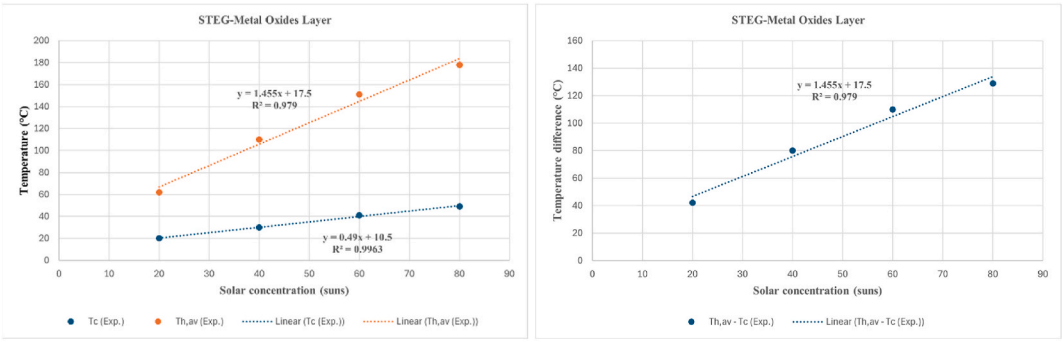

(a) (b)

Fig. 15. Variation of (a) hot-side and cold-side temperatures and (b) temperature difference as a function of solar concentration for the metal oxides layer (MOL)-based solar thermoelectric generator (STEG).

at 20 suns and 0.6 % at 40 suns). However, at higher irradiance (60 and 80 suns), the discrepancies increased to 13.8 % and 41.7 %, respectively.

As for η, the differences between simulated and experimental values were relatively small at lower irradiance levels (2.1 % at 20 suns and 1.7 % at 40 suns). However, at higher irradiance (60 and 80 suns), the discrepancies increased to 9.5 % and 28.5 %, respectively.

Similarly, at each irradiation level, the discrepancy between the simulated and experimental I_{sc} and V_{oc} values could be attributed

Table 7
RMSE error metric calculated between experimental and simulated maximum power output (P_{max}) results for the graphite sheet (GS)-based solar thermoelectric generator (STEG).

	GS-based STEG		RMSE
	Experimental P_{max} (W)	Simulated P_{max} (W)	
20	0.308	0.314	0.45
40	1.120	1.142	
60	1.984	2.251	
80	2.670	3.535	

Table 8
RMSE error metric calculated between experimental and simulated maximum power output (P_{max}) results for the metal oxides layer (MOL)-based solar thermoelectric generator (STEG).

	MOL-based STEG		RMSE
	Experimental P_{max} (W)	Simulated P_{max} (W)	
20	0.559	0.523	0.81
40	1.818	1.829	
60	3.071	3.495	
80	3.762	5.330	

to differences in the measured and simulated conditions. Specifically, the simulated I_{sc} values were not obtained at $V_{oc} = 0$ V because $R = 0$ is undefined for the electrical load in the numerical model. Instead, a non-zero resistance ($R \neq 0$) was set for the electrical load in the simulations, leading to consistently lower simulated I_{sc} values compared to the experimental ones.

Once again, the variations in the differences between simulated and experimental P_{max} and η values across irradiation levels could be attributed to temperature nonuniformities, which become more pronounced as irradiation levels increase. In real-world conditions, these nonuniformities arise from irradiance fluctuations, whereas the simulations did not account for them. Despite this, the simulations overall show good agreement with the experimental data.

3.3. Quantitative metrics

For both the GS-based STEG and the MOL-based STEG, the relationship between P_{max} and solar concentration was evaluated for both experimental and simulation cases, as shown in Figs. 12 and 13, respectively. In the experimental case, the coefficient of determination (R^2) was 0.9979 for the GS-based STEG and 0.984 for the MOL-based STEG. In the simulation case, the R^2 was 0.991 for the GS-based STEG and 0.9945 for the MOL-based STEG. These results indicate a strong linear dependence between P_{max} and solar concentration for both experimental and simulation data.

For both the GS-based STEG and the MOL-based STEG, the relationship between solar concentration and hot-side and cold-side temperatures, as well as the relationship between solar concentration and temperature difference, were evaluated based on experimental data only. These results are shown in Figs. 14 and 15. For the hot-side and cold-side temperatures, the coefficient of determination (R^2) was 0.9959 and 0.9963, respectively, for the GS-based STEG, and 0.979 and 0.9963, respectively, for the MOL-based STEG. For the temperature difference, the R^2 was 0.9868 for the GS-based STEG and 0.979 for the MOL-based STEG. These results indicate a strong linear dependence between solar concentration and both hot-side and cold-side temperatures, as well as the temperature difference, for both the GS-based STEG and the MOL-based STEG.

The Root Mean Square Error (RMSE) error metric was calculated to evaluate the agreement between the simulation and experimental results. It was calculated for the experimental and simulated P_{max} values for both the GS-based STEG and the MOL-based STEG, as shown in Tables 7 and 8, respectively. The RMSE values were 0.4 for the GS-based STEG and 0.8 for the MOL-based STEG, indicating a good match between the experimental and simulated P_{max} results.

3.4. Comparative analysis

Table 9 presents a comparative analysis of the output performance of various STEGs against the STEG investigated in this study. The STEG reported in Ref. [24], despite utilizing the same light absorber (GS) and operating under a higher solar concentration (107 suns), exhibited inferior performance across all key metrics, including I_{sc}, V_{oc}, P_{max}, and η. Specifically, its efficiency was 88.5 % lower than that of the GS-based STEG under 40 suns and 79 % lower than the MOL-based STEG under 20 suns in the present study.

The STEG described in Ref. [28], which employed a Candle Soot (CS) absorber at a solar concentration of 60 suns, also showed lower performance across most metrics (I_{sc}, V_{oc}, and P_{max}) compared to the GS-based and MOL-based STEGs under 20 suns in this study. Although the CS-based STEG achieved a relatively high efficiency (6.3 %) compared to the GS-based and MOL-based STEGs, its practical application is hindered by challenges such as the limited absorption capacity of CS materials across the broad spectral range of 0.3–2.5 μm and poor adhesion properties on the device's hot-side surface [44].

The STEG from Ref. [29], which utilized a GS absorber at a solar concentration of 56 suns, exhibited a relatively low maximum

Table 9
Comparison of STEG output performance between this study and previous research.

Sources	Publication's year	Solar absorber	Thermoelectric module	Cooling method	Heating source	Concentrator	Concentration rate (suns)	P_{in} (W)	I_{sc} (A)	V_{oc} (V)	P_{max} (W)	η (%)	Sim./ Exp
Mahmoudinezhad et al. [24]	2018	GS	CMO-25-42S (50 $CaMnO_3$ n-type and $Ca_3Co_4O_3$ p-type leg pairs)	Water-cooled heat sink	Xenon lamp	–	107	189	1.21	1.56	0.45	0.2	Exp.
Yadav et al. [28]	2020	CS[a]	TEC1-12706 (127 Bi_2Te_3 leg pairs)	Water-cooled heat sink	Solar radiation	Fresnel lens	60	96	0.01	1.50	0.01	6.3	Exp.
Mahmoudinezhad et al. [29]	2020	GS	TEG2-07025HT-SS (199 Bi_2Te_3 leg pairs)	Water-cooled heat sink	Xenon lamp	–	56	90	NA	NA	1.82	3.3	Exp.
Xuan et al. [45]	2024	NA	TEG model (128 $CoSb_3$ leg pairs)	Water-cooled heat sink (Cold-end heat transfer coefficient h_c = 10000 W/m^2)	Nonuniform solar radiation model (using 2-D Gaussian distribution with $D^2 = 0.2 \times 10^{-4}$)	–	60	96	NA	NA	3.04	3.16	Sim.
Present work	–	GS	TEC1-12710 (127 Bi_2Te_3 leg pairs)	Water-cooled heat sink	Xenon lamp	–	20	32	0.710	1.831	0.308	0.96	Exp.
		MOL							0.938	2.496	0.559	1.75	
		GS					40	64	1.267	3.482	1.120	1.75	
		MOL							1.557	4.655	1.818	2.84	
		GS					60	96	1.602	4.854	1.984	2.1	
		MOL							1.896	6.430	3.071	3.2	
		GS					80	128	1.786	5.555	2.670	2.1	
		MOL							2.058	7.316	3.762	2.94	

[a] CS: Candle Soot.

power output (8 %) but a comparatively high efficiency (36 %) relative to the GS-based STEG under 60 suns. It also demonstrated equivalent maximum power output and efficiency to the MOL-based STEG under 40 suns.

The STEG from Ref. [45], simulated at a solar concentration of 60 suns, exhibited comparable maximum power output and efficiency to the proposed MOL-based STEG under identical illumination conditions. However, Bismuth Telluride (Bi_2Te_3) demonstrates superior performance in low-temperature applications (below 200 °C), while Skutterudite ($CoSb_3$) is more suitable for high-temperature applications in the range of 200 °C–600 °C.

In summary, the comparative analysis highlights the significant performance enhancement of the STEG integrated with a MOL absorber. This improvement is attributed to the MOL's superior thermal energy absorption capacity under concentrated solar radiation, as demonstrated in this study.

4. Conclusion

Solar Thermoelectric Generators (STEGs) are promising candidates for sustainable energy production, with ongoing efforts to enhance their efficiency through advanced thermal absorbers and accurate numerical modeling. This study investigated the performance of STEGs incorporating graphite sheet (GS) and metal oxide layer (MOL) absorbers under concentrated solar radiation using both simulations and experiments.

Using COMSOL Multiphysics, simulations modeled STEGs at solar irradiance levels of 20, 40, 60, and 80 suns, with corresponding cold-side temperatures of 20 °C, 30 °C, 41 °C, and 49 °C. The three-dimensional numerical models included the temperature-dependent thermoelectric properties of Bismuth Telluride (Bi_2Te_3) legs and material properties of alumina ceramic plates, copper interconnectors, and absorbers.

Experimentally, Xenon lamps, TEC1-12710 thermoelectric modules coated with GS and MOL absorbers, and water-cooled copper heat sinks were employed. Key parameters such as short-circuit current, open-circuit voltage, maximum power output, and efficiency were measured and compared with simulation results.

The MOL-based STEG outperformed the GS-based configuration across all metrics, significantly enhancing maximum power output and efficiency. For instance, at 60 suns, the MOL-based STEG generated 3.071 W (3.2 %), compared to 1.984 W (2.1 %) for the GS-based STEG, with efficiency improvements of approximately 52 %. Additionally, the MOL-based STEG also demonstrated the potential for compact designs by surpassing the GS-based STEG's performance at higher irradiance levels.

Comparisons between experimental and simulation results revealed minor discrepancies at lower irradiance levels, but larger deviations at higher levels, likely due to temperature nonuniformities and real-world irradiance fluctuations not accounted for in the simulations. Nonetheless, strong linear relationships were observed between maximum power, hot-side temperature, cold-side temperature, and temperature difference (ΔT) with solar concentration, confirmed by high coefficients of determination (R^2) for both STEG configurations. Moreover, low RMSE error values between simulated and experimental maximum power outputs, for both STEG configurations, further confirming the validity of the models. This study also highlighted the advantages of MOL absorbers in enhancing STEG performance over other absorbers.

This work focused on steady-state conditions, excluding transient analyses, environmental factors (e.g., ambient temperature, wind, and humidity), and the effects of long-term reliability and material degradation. Additionally, the numerical models did not incorporate a water-cooled copper heat sink and did not test under unconcentrated solar irradiance conditions. Addressing these factors in future studies is critical for further optimization and broader application of STEGs.

Future research should explore novel spectrally selective absorbers (SSAs) with higher solar absorbance and advanced thermoelectric materials with improved figures of merit. Investigating unconcentrated solar irradiance conditions and optimizing the design and geometry of thermoelectric modules could further enhance performance. Moreover, integrating machine learning and artificial intelligence techniques to optimize operational parameters could unlock smarter and more efficient STEG systems.

CRediT authorship contribution statement

Abdelkader Rjafallah: Writing – review & editing, Writing – original draft, Visualization, Software, Methodology, Investigation, Formal analysis, Conceptualization. **Daniel Tudor Cotfas:** Writing – review & editing, Validation, Supervision, Project administration, Methodology, Investigation, Formal analysis, Data curation, Conceptualization. **Petru Adrian Cotfas:** Writing – review & editing, Visualization, Validation, Supervision, Project administration, Methodology, Investigation, Formal analysis, Data curation, Conceptualization.

Declaration of competing interest

The authors declare that they have no known competing financial interests or personal relationships that could have appeared to influence the work reported in this paper.

Acknowledgments

The authors gratefully acknowledge the support of the Ministry of Research, Innovation, and Digitization, CNCS-UEFISCDI, through grant number PN-III-P4-PCE-2021-1020 (PCE87), within PNCDI III. Special thanks are extended to the IMDEA Energy Institute for access to its facilities, as well as to its scientific and technical staff for their invaluable assistance. Financial support from

the SFERA-III project (Grant Agreement No. 823802) is also appreciated.

Data availability

Data will be made available on request.

References

[1] M. Derraz, C. Ennawaoui, H. Mastouri, Y. El Hmamssy, N. Abouricha, A. Rjafallah, E.M. Laadissi, A. Hajjaji, Mathematical modeling for predicting electrical energy harvested using piezoelectric composite materials for smart system applications, Micro Nano Eng 23 (2024) 100253, https://doi.org/10.1016/j.mne.2024.100253.
[2] S. Ozbektas, A. Kaleli, B. Sungur, Prediction of the effect of load resistance and heat input on the performance of thermoelectric generator using numerical and artificial neural network models, Appl. Therm. Eng. 249 (2024) 123417, https://doi.org/10.1016/j.applthermaleng.2024.123417.
[3] D. Sanin-Villa, O.D. Montoya, L.F. Grisales-Noreña, Material property characterization and parameter estimation of thermoelectric generator by using a master–slave strategy based on metaheuristics techniques, Mathematics 11 (2023) 1326, https://doi.org/10.3390/math11061326.
[4] S.O. Salawu, A.M. Obalalu, E.O. Fatunmbi, R.A. Oderinu, Thermal Prandtl-Eyring hybridized MoS2-SiO2/C3H8O2 and SiO2-C3H8O2 nanofluids for effective solar energy absorber and entropy optimization: a solar water pump implementation, J. Mol. Liq. 361 (2022) 119608, https://doi.org/10.1016/j.molliq.2022.119608.
[5] P.A. Cotfas, D.T. Cotfas, Comprehensive review of methods and instruments for photovoltaic–thermoelectric generator hybrid system characterization, Energies 13 (2020) 6045, https://doi.org/10.3390/en13226045.
[6] A.M. Obalalu, T. Oreyeni, A. Abbas, M.A. Memon, U. Khan, E.-S.M. Sherif, A.M. Hassan, I. Pop, Implication of electromagnetohydrodynamic and heat transfer analysis in nanomaterial flow over a stretched surface: applications in solar energy, Case Stud. Therm. Eng. 49 (2023) 103381, https://doi.org/10.1016/j.csite.2023.103381.
[7] D.T. Cotfas, P.A. Cotfas, Enhancing energy efficiency for photovoltaic cells using thermoelectric hybridization, in: 2020 5th Int. Conf. Smart Sustain. Technol. Split, 2020, pp. 1–6, https://doi.org/10.23919/SpliTech49282.2020.9243852.
[8] A. Younis, A. Rjafallah, P.A. Cotfas, D.T. Cotfas, Dust impact on electrical and thermal photovoltaic performance: insights from field and laboratory experiments, Energy Rep. 11 (2024) 2099–2110, https://doi.org/10.1016/j.egyr.2024.01.065.
[9] L. Zaghba, M. Khennane Benbitour, A. Fezzani, S. Mekhilef, A. Borni, Investigating the theoretical and experimental effects of sand dust and sandstorms on photovoltaic power plants in arid environments, Energy Sustain. Dev. 81 (2024) 101507, https://doi.org/10.1016/j.esd.2024.101507.
[10] H.A. Zaharil, H. Yang, Novel solar-based cogeneration system: parabolic trough integrating supercritical Brayton and organic Rankine cycles with membrane distillation, Appl. Energy 376 (2024) 124210, https://doi.org/10.1016/j.apenergy.2024.124210.
[11] A.M. Obalalu, M.O. Oni, U. Khan, A. Abbas, T. Muhammad, A. Zaib, Two-phase numerical simulation for the heat and mass transfer evaluation across a vertical deformable sheet with significant impact of solar radiation and heat source/sink, Arab. J. Sci. Eng. 49 (2024) 11053–11071, https://doi.org/10.1007/s13369-023-08585-z.
[12] S.O. Salawu, A.M. Obalalu, M.D. Shamshuddin, Nonlinear solar thermal radiation efficiency and energy optimization for magnetized hybrid Prandtl–eyring nanoliquid in aircraft, Arab. J. Sci. Eng. 48 (2023) 3061–3072, https://doi.org/10.1007/s13369-022-07080-1.
[13] A.M. Obalalu, L.L. Adebayo, I. Colak, A.O. Ajala, F.A. Wahaab, Entropy generation minimization on electromagnetohydrodynamic radiative Casson nanofluid flow over a melting Riga plate, Heat Transf. 51 (2022) 3951–3978, https://doi.org/10.1002/htj.22484.
[14] A.M. Obalalu, Heat and mass transfer in an unsteady squeezed Casson fluid flow with novel thermophysical properties: analytical and numerical solution, Heat Transf. 50 (2021) 7988–8011, https://doi.org/10.1002/htj.22263.
[15] S.S. Joshi, A.S. Dhoble, Photovoltaic -Thermal systems (PVT): technology review and future trends, Renew. Sustain. Energy Rev. 92 (2018) 848–882, https://doi.org/10.1016/j.rser.2018.04.067.
[16] A. Rjafallah, A. Younis, D.T. Cotfas, P.A. Cotfas, Effects of temperature uniformity and nonuniformity on thermoelectric generator performance across hot and cold sides, Case Stud. Therm. Eng. 59 (2024) 104596, https://doi.org/10.1016/j.csite.2024.104596.
[17] Al Khalil, S. Sahnoun, A. Elhassnaoui, S. Yadir, A. Obbadi, Y. Errami, Solar thermoelectric generator and thermoelectric cooler performance: analysis and comparison using a different shape geometry, Clean Energy 7 (2023) 1233–1246, https://doi.org/10.1093/ce/zkad067.
[18] S.A. Alsibiani, Experimental study of an optical concentrated solar thermoelectric power generator, Ain Shams Eng. J. 15 (2024) 102380, https://doi.org/10.1016/j.asej.2023.102380.
[19] W. Jing, Y. Ji, Y. Xie, Q. Lai, G. Wu, B. Xie, C. Wang, J. Tan, Enhancing thermoelectric generation: integrating passive radiative cooling and concentrated solar heating with consideration of parasitic heat conduction, Case Stud. Therm. Eng. 62 (2024) 105232, https://doi.org/10.1016/j.csite.2024.105232.
[20] L. Amiri, C.-T. Liang, A. Narjis, A. Alsaad, Geometry optimization of a thermoelectric generator with temperature-dependent properties, Appl. Phys. A 130 (2024) 447, https://doi.org/10.1007/s00339-024-07614-4.
[21] O.Y. Enciso-Montes de Oca, M.A. Olivares-Robles, Dynamic performance optimization of two-stage thermoelectric generator: impact of different geometric leg shapes in each stage, Energy Rep. 11 (2024) 597–610, https://doi.org/10.1016/j.egyr.2023.12.032.
[22] A. Rjafallah, D.T. Cotfas, P.A. Cotfas, Investigation of temperature variations across the hot and cold sides of cascaded thermoelectric generator (CTEG) configurations in PV-CTEG hybrid systems, Case Stud. Therm. Eng. 61 (2024) 105070, https://doi.org/10.1016/j.csite.2024.105070.
[23] E. Azizi, Z. Khalili, M. Sheikholeslami, Simulation of solar photovoltaic system integrated with TEG in presence of hybrid nanomaterial, J. Therm. Anal. Calorim. 149 (2024) 5771–5782, https://doi.org/10.1007/s10973-024-13192-7.
[24] S. Mahmoudinezhad, P.A. Cotfas, D.T. Cotfas, A. Rezania, L.A. Rosendah, Performance evaluation of a high-temperature thermoelectric generator under different solar concentrations, Energy Proc. 147 (2018) 624–630, https://doi.org/10.1016/j.egypro.2018.07.080.
[25] J. Wang, Z.-Y. Wang, E.-T. Hu, Q.-Y. Cai, K.-H. Yu, W. Wei, Enhanced electrical outputs of thin-film solar thermoelectric generator with optimized metal/dielectric multilayered solar selective absorber, Appl. Phys. A 128 (2022) 572, https://doi.org/10.1007/s00339-022-05713-8.
[26] J. Zhang, C. Wang, J. Shi, D. Wei, H. Zhao, C. Ma, Solar selective absorber for emerging sustainable applications, Adv. Energy Sustain. Res. 3 (2022) 2100195, https://doi.org/10.1002/aesr.202100195.
[27] D. Kraemer, B. Poudel, H.-P. Feng, J.C. Caylor, B. Yu, X. Yan, Y. Ma, X. Wang, D. Wang, A. Muto, K. McEnaney, M. Chiesa, Z. Ren, G. Chen, High-performance flat-panel solar thermoelectric generators with high thermal concentration, Nat. Mater. 10 (2011) 532–538, https://doi.org/10.1038/nmat3013.
[28] D. Yadav, P. Azad, R. Vaish, Solar energy harvesting using candle-soot-coated thermoelectric materials, Glob. Chall. 4 (2020) 1900080, https://doi.org/10.1002/gch2.201900080.
[29] S. Mahmoudinezhad, P.A. Cotfas, D.T. Cotfas, L.A. Rosendahl, A. Rezania, Response of thermoelectric generators to Bi2Te3 and Zn4Sb3 energy harvester materials under variant solar radiation, Renew. Energy 146 (2020) 2488–2498, https://doi.org/10.1016/j.renene.2019.08.080.
[30] V. Silva Oliveira, M.M. Camboim, C. Protasio de Souza, B.A. Silva Guedes de Lima, O. Baiocchi, H.-S. Kim, A thermoelectric energy harvester based on microstructured quasicrystalline solar absorber, Micromachines 12 (2021) 393, https://doi.org/10.3390/mi12040393.
[31] Z. Sun, D. Luo, R. Wang, Y. Li, Y. Yan, Z. Cheng, J. Chen, Evaluation of energy recovery potential of solar thermoelectric generators using a three-dimensional transient numerical model, Energy 256 (2022) 124667, https://doi.org/10.1016/j.energy.2022.124667.
[32] M. Jaegle, Multiphysics simulation of thermoelectric systems - modeling of peltier - cooling and thermoelectric generation, in: COMSOL Conf. 2008 Hann, 2008.
[33] COMSOL Multiphysics, (n.d.). https://www.comsol.com.

[34] B.T. Admasu, X.B. Luo, J.W. Yao, T.Z. Ming, Effects of non-uniform hot junction temperature distribution on the outputs of thermoelectric power generation system, Appl. Mech. Mater. 283 (2013) 87–97. https://doi.org/10.4028/www.scientific.net/AMM.283.87.
[35] D. Luo, Z. Liu, Y. Yan, Y. Li, R. Wang, L. Zhang, X. Yang, Recent advances in modeling and simulation of thermoelectric power generation, Energy Convers. Manag. 273 (2022) 116389, https://doi.org/10.1016/j.enconman.2022.116389.
[36] S. Shittu, G. Li, X. Zhao, X. Ma, Y.G. Akhlaghi, E. Ayodele, Optimized high performance thermoelectric generator with combined segmented and asymmetrical legs under pulsed heat input power, J. Power Sources 428 (2019) 53–66, https://doi.org/10.1016/j.jpowsour.2019.04.099.
[37] H.R. Fallah Kohan, F. Lotfipour, M. Eslami, Numerical simulation of a photovoltaic thermoelectric hybrid power generation system, Sol. Energy 174 (2018) 537–548, https://doi.org/10.1016/j.solener.2018.09.046.
[38] A. Prasad, R.C. Thiagarajan, Multiphysics modelling and multilevel optimization of thermoelectric generator for waste heat recovery, in: ITC Gardenia, 2018. https://api.semanticscholar.org/CorpusID:231771951.
[39] M. Baneto, A. Enesca, C. Mihoreanu, Y. Lare, K. Jondo, K. Napo, A. Duta, Effects of the growth temperature on the properties of spray deposited CuInS2 thin films for photovoltaic applications, Ceram. Int. 41 (2015) 4742–4749, https://doi.org/10.1016/j.ceramint.2014.12.023.
[40] D.T. Cotfas, A. Enesca, P.A. Cotfas, Enhancing the performance of the solar thermoelectric generator in unconcentrated and concentrated light, Renew. Energy 221 (2024) 119831, https://doi.org/10.1016/j.renene.2023.119831.
[41] A. Enesca, V. Sisman, UV–Vis activated CuO/CuS/WO3@PANI heterostructure for photocatalytic removal of pharmaceutical active compounds, Ceram. Int. 49 (2023) 30592–30602, https://doi.org/10.1016/j.ceramint.2023.07.012.
[42] P.A. Cotfas, D.T. Cotfas, Solar hybrid system component study in low concentrated sunlight, Int. J. Photoenergy 2021 (2021) 6677473, https://doi.org/10.1155/2021/6677473.
[43] L.L. Baranowski, G.J. Snyder, E.S. Toberer, Concentrated solar thermoelectric generators, Energy Environ. Sci. 5 (2012) 9055–9067, https://doi.org/10.1039/C2EE22248E.
[44] P. Ma, Y. Wang, X. Zhang, B. Yang, J. Lang, J. Yang, Z. Wang, A. Abdukayumb, G. Hu, Photothermal conversion-enhanced thermoelectric generators combined with supercapacitors: an efficacious approach to integrated power generation and storage, Chem. Eng. J. 492 (2024) 152406, https://doi.org/10.1016/j.cej.2024.152406.
[45] Z. Xuan, M. Ge, C. Zhao, Y. Li, S. Wang, Y. Zhao, Effect of nonuniform solar radiation on the performance of solar thermoelectric generators, Energy 290 (2024) 130249, https://doi.org/10.1016/j.energy.2024.130249.